ACS APPLIED OPTICAL MATERIALS

pubs.acs.org/acsaom Article

Visualizing Local Superconductivity of NbTiN Nanowires to Probe Inhomogeneity in Single-Photon Detectors

Pei-Jung Chen, Guan-Hao Chen, Robert Vedin, Mattias Jönsson, Samuel Gyger, Stephan Steinhauer, Juhn-Jong Lin, Wen-Hao Chang, Jack Lidmar, Val Zwiller,* and Chun-Liang Lin*

Cite This: ACS Appl. Opt. Mater. 2024, 2, 68−75 Read Online

ACCESS | Metrics & More | Article Recommendations | Supporting Information

ABSTRACT: NbTiN has a high critical temperature (T_c) of up to 17 K, making it a great candidate for superconducting nanowire single-photon detectors (SNSPDs) and other applications requiring a bias current close to the depairing current. However, superconducting inhomogeneities are often observed in superconducting thin films, and superconducting inhomogeneities can influence the vortex nucleation barrier and furthermore affect the critical current I_c of a superconducting wire. Superconducting inhomogeneities can also result in stochastic variations in the critical current between identical devices, and therefore, it is crucial to have a detailed understanding of inhomogeneities in SNSPDs in order to improve device efficiency. In this study, we utilized scanning tunneling microscopy/spectroscopy (STM/STS) to investigate the inhomogeneity of superconducting properties in meandered NbTiN nanowires, which are commonly used in SNSPDs. Our findings show that variations in the superconducting gap are strongly correlated with the film thickness. By using time-dependent Ginzburg−Landau simulations and statistical modeling, we explored the implications of the reduction in the critical current and its sample-to-sample variations. Our study suggests that the thickness of NbTiN plays a critical role in achieving homogeneity in superconducting properties.

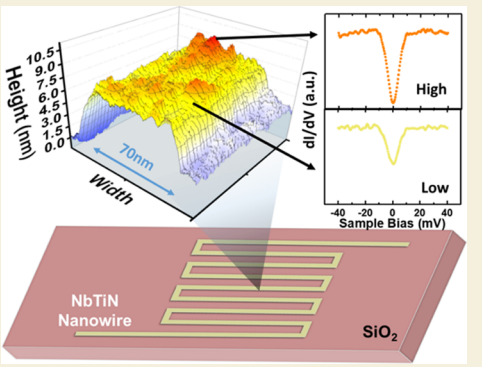

KEYWORDS: *single-photon detector, superconducting nanowire, NbTiN, inhomogeneity superconducting properties*

INTRODUCTION

Nanoscale devices based on superconducting thin films are essential components of modern quantum technologies, as demonstrated in a variety of applications including superconducting[1,2] and photonic quantum computing,[3] quantum sensing of single spin excitations,[4] and high-fidelity quantum communication.[5] In recent experiments, superconducting nanowire single-photon detectors (SNSPDs) have been used to detect visible or infrared photons with high detection efficiencies approaching unity,[6,7] sub-3 ps temporal resolution,[8] and milli-Hertz dark count rates.[9,10] The performance of SNSPDs critically depends on the local inhomogeneity and spatial variations of the superconducting properties in the thin film material.

Disorder in superconducting thin films is primarily influenced by the growth method used, such as molecular-beam epitaxy,[11] chemical vapor deposition,[12] atomic layer deposition,[13] and magnetron sputtering.[14] Among these techniques, magnetron sputtering is the most widely used for superconducting device fabrication. The resulting level of inhomogeneity has often been difficult to discern, but it would have a considerable impact on the device properties. Multiple studies have demonstrated that disorder-driven effects in superconducting thin films, such as superconductor-insulator transitions,[15] disorder-induced phases,[16] spatially inhomogeneous superconductivity,[17−19] the edge of nanowires induced can arise due to even the slightest degree of disorder, leading to variations in the superconducting gap (Δ) and critical temperature (T_c).[20]

Superconducting devices, such as SNSPDs, are often operated with bias currents that are close to the depairing current. However, material inhomogeneity can affect the vortex nucleation barrier, leading to stochastic variations in the critical currents (I_c) of other identical devices. A recent study points out that smooth edges are critical for obtaining a high critical current due to it owing a higher maximal vortex velocity and shorter energy relaxation times (τ) compared to strips with rough edges.[21] For instance, experimental studies have shown that an overall reduction in I_c is observed as wire lengths increase.[22,23] To realize high-performance superconducting devices,[24−27] including SNSPDs with high detection efficiency and excellent temporal resolution,[28] niobium-based nitrides are widely used materials.[29] Previous studies have demonstrated

Received: September 13, 2023
Revised: December 9, 2023
Accepted: December 11, 2023
Published: December 27, 2023

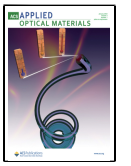

https://doi.org/10.1021/acsaom.3c00326
ACS Appl. Opt. Mater. 2024, 2, 68−75

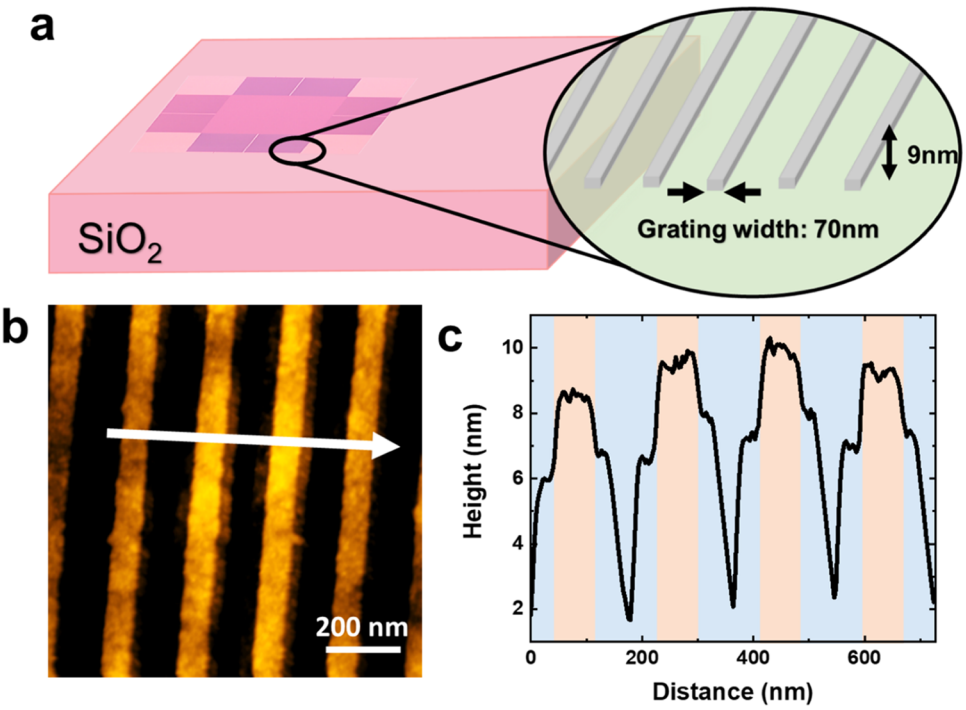

Figure 1. STM characterization of the nanowires structure. (a) Schematic diagram of a patterned NbTiN on SiO_2. The inset shows the structure of nanowires. (b) Large-scale STM image that shows the nanowire structure (1000 nm × 1000 nm, $V_s = -1.0$ V, $I_t = 1.0$ nA). (c) Line profile taken along the white arrow in panel (b). Width of NbTiN nanowires is 70 nm, as shaded by the orange region.

that NbTiN, a ternary compound, exhibits considerable disorder that affects properties such as critical temperature (T_c) and I_c.[30−33] In addition to microscopic parameters such as film thickness, grain sizes, and point defects, the Nb/Ti ratio can be adjusted to tune the composition of the material, which can have an impact on the superconducting properties and, ultimately, the performance of SNSPDs.[34]

In this study, we used STM/STS to investigate the superconducting properties of meandered NbTiN nanowires commonly used in superconducting quantum devices. We analyze the local superconductivity and observe that the depth of Δvaries across the NbTiN nanowires. The further examination reveals a strong correlation between the variation of the superconducting gap and the local film thickness. By incorporating microscopic characterization of the superconducting inhomogeneity into time-dependent Ginzburg−Landau simulations, we can quantify reductions in critical current compared to the depairing current in a material with a statistically fluctuating disorder. We deduce that scaling laws of NbTiN critical currents are a function of wire length and correlate them with experimentally observed data. Overall, our findings provide important insights into the superconducting properties of meandering NbTiN nanowires and their performance in superconducting quantum devices.

EXPERIMENTAL METHOD

The devices were fabricated on a silicon substrate that was covered with a layer of thermally grown SiO_2 with a measured thickness of 250 nm. A 9 nm thick film of NbTiN was deposited using a reactive sputtering process.[34] To pattern the film into 70 nm wide parallel nanowires, e-beam lithography (Microresist ma-N 2401) and reactive ion etching based on CF_4/O_2 chemistry were used. The resist was then stripped overnight (Microresist mr-Rem 700). For the NbTiN nanowires used in critical current measurements at 2.5 K, the same fabrication process was followed, but the resist stripping step was omitted. In this case, a device configuration consisting of a single 100 nm wide strip connected to two contact pads was chosen. Critical current measurements were carried out using a commercial single-photon detector from Single Quantum B.V.

To prepare the meandered NbTiN nanowires for STM/STS measurements, the nanowires were introduced into the UHV chamber at a base pressure of 2×10^{-10} torr. The surface was then cleaned by Ar^+ ion-bombardment at 0.3 keV for 10 min, followed by annealing at 120 °C for 15 min (2 cycles). After carrying out the surface treatment, the surface roughness remained almost the same. (The surface still has particle grain-like features but the large-scale surface roughness before/after is 153/121 pm.) The STM/STS measurements were conducted under a liquid He condition, and the STM images were acquired in constant current mode. The STM tips were made of tungsten, which was prepared by electrochemical etching in a 3 M NaOH solution. STS was carried out using a lock-in amplifier operating at 687.7 Hz with a 400 μV modulation.

The dynamics of the superconducting wire is described by a 2D (generalized) time-dependent Ginzburg−Landau (GTDGL) model[35−37] in zero magnetic field

$$\frac{u}{\sqrt{1+\gamma^2|\psi|^2}}\left(\frac{\partial}{\partial t}+i\mu+\frac{\gamma^2}{2}\frac{\partial|\psi|^2}{\partial t}\right)\psi = \xi^2\nabla^2\psi-(|\psi|^2-|\Delta(\mathbf{r})/\Delta_0|^2)\psi \quad (1)$$

$$\nabla^2\mu = \nabla\cdot\mathrm{Im}[\psi^*\nabla\psi] \quad (2)$$

in reduced units, ψ is the superconducting order parameter whose nominal size is proportional to the superconducting gap $\Delta(\mathbf{r})/\Delta_0$; μ is the electric potential; ξ is the superconducting coherence length; and γ is proportional to the inelastic electron−phonon scattering time. u is the ratio of relaxation times for the order parameter and the current in dirty superconductors. We set $u = 5.79$ and $\gamma = 10$. The disorder of the film is encoded as a random local gap $\Delta(\mathbf{r})$. The spatial correlations of the disorder are implemented as a set of randomly generated convex domains, each with independent random $\Delta(\mathbf{r})$ values drawn from a normal distribution with relative standard deviation σ. These convex domains are generated using the

https://doi.org/10.1021/acsaom.3c00326
ACS Appl. Opt. Mater. 2024, 2, 68−75

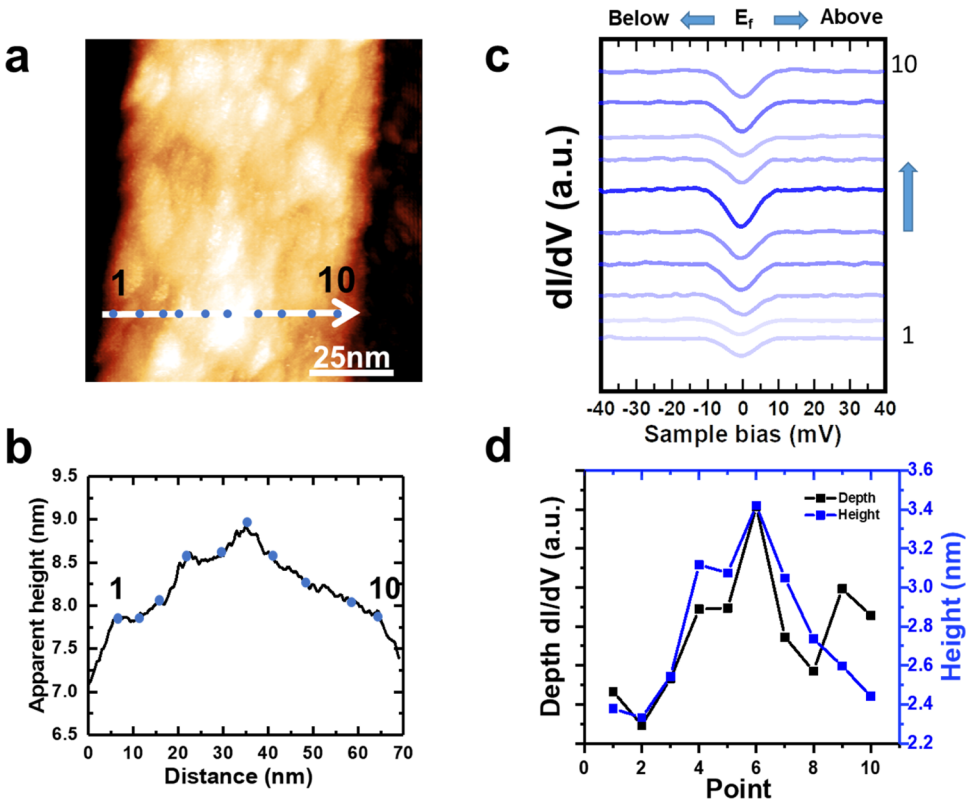

Figure 2. STS spectra taken along with nanowires. (a) STM image of a single nanowire in 100 nm × 100 nm size at 4.9 K (V_s = − 1.0 V, I_t = 1.0 nA). (b) Line profile along the points on the white arrow given in panel (a). (c) Plot of all the dI/dV spectra acquired at the points in (a) across the NbTiN nanowire. The gradient color indicates the depth of superconducting gap. (d) Dual plot showing the depth of the superconducting gap and relative heights along with the points in (a).

microstructpy package,[38,39] giving a distribution for the domain size d as the input. With this model, we simulate the critical current distribution for a rectangular superconducting geometry $W \times L_1$, see Figure 4a, with typical width $W = 20\ \xi$ and length $L_1 = 100\ \xi$. Lengths are measured in units of the superconducting coherence length, which for the NbTiN films has been determined to be $\xi \approx 4-5$ nm.[30] A bias current density J_b is injected and extracted as normal currents on the left and right edges via a boundary condition $\psi = 0$, $\hat{x}\cdot\nabla\mu = J_b$ applied to a surrounding buffer zone of $W \times 10\ \xi$ on either side. The presence of the buffer zones allows the order parameter to recover while the normal current transforms to supercurrent. For the isolating boundaries along the wire at $y = \pm\frac{W}{2}$ the boundary conditions $\hat{y}\cdot\nabla\psi = 0$, $\hat{y}\cdot\nabla\mu = 0$ are used. The critical currents are extracted, similarly to ref 40, from IV curves simulated by using around 5000 different realizations of the disorder configuration, giving an empirical probability distribution P_1 (I_c).

RESULTS AND DISCUSSION

The structure of the NbTiN film on SiO_2 used for STM/STS imaging is shown in Figure 1a. The film is 9 nm thick and has a square shape that is surrounded by eight patterned areas, consisting of the same material and thickness. The middle pad structure is an aim for us to locate the NbTiN thin film due to the poor optical resolution of CCD installed in STM (Figure S1). The patterned areas consist of structures with 70 nm wide NbTiN nanowires separated by 110 nm. The schematic of the nanowires structures is shown in the inset of Figure 1a. A large-scale STM image of the area with the strip structures is presented in Figure 1b, while Figure 1c shows the line profile along the direction of the white arrow in Figure 1b. The line profile clearly shows the height and width of the strip structures. These nanowire configurations are commonly used in SNSPD devices.[34,41]

Figure 2a displays an STM image of a single nanowire in the strip areas, exhibiting an inhomogeneous height. Figure 2b shows the corresponding line profile across the white arrow in Figure 2a. The STS spectra corresponding to the positions labeled in Figure 2a are demonstrated in Figure 2c. All STS spectra exhibit a clear gap near the Fermi level, indicating superconducting behavior. However, the NbTiN thin film is a disordered superconducting material, and it has been shown that the coherence peak is hard to define.[42] To determine T_c, we introduce zero-bias conductance (ZBC) to be an index for comparing the T_c because as the temperature increases, thermal fluctuations can break up Cooper pairs and create free electrons, which reduces the number of available states in the energy gap and decreases the depth of the dip, indicating these two properties are correlated. The ZBC is the deepest point in the spectrum. The depth and width of the superconducting gap vary among the measuring points, revealing the inhomogeneous properties along the nanowire. To further understand the reason leading to this superconducting inhomogeneity, the film thickness is considered. Figure 2d shows the extracted depth of the superconducting gap and relative heights from each measuring point, revealing a strong correlation between them.

To confirm the presence of superconducting inhomogeneity in NbTiN nanowires, a similar measurement was performed on an unpatterned NbTiN film of the same thickness. The STM topographic image (30 × 30 nm) of the unpatterned NbTiN film with a relatively large corrugation is shown in Figure 3a.

https://doi.org/10.1021/acsaom.3c00326
ACS Appl. Opt. Mater. 2024, 2, 68−75

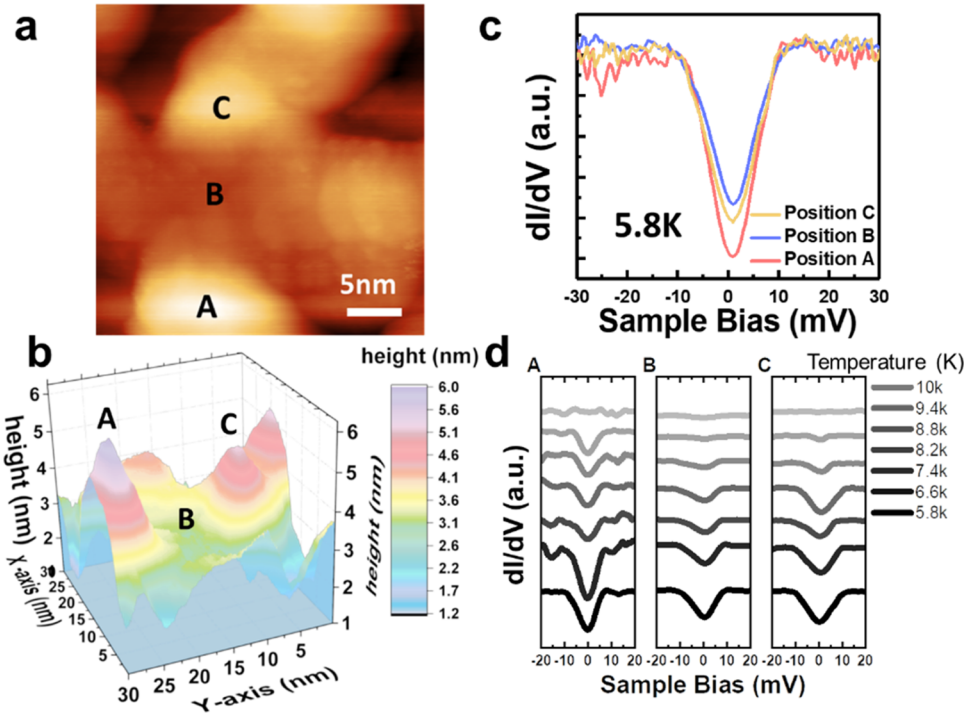

Figure 3. Temperature-dependent STS spectra in NbTiN thin film. (a) STM image in 30 nm × 30 nm size of NbTiN thin film at 5.8 K (V_s = − 1.0 V, I_t = 1.0 nA). (b) A 3D plot of the STM image in panel (a). (c) STS spectra measured on A, B, and C in panels (a) and (b) at 5.8 K. (d) Temperature-dependent STS spectra taken at points A, B, and C.

The large-scale image is shown in Figure S2. The height difference between points A and C is emphasized in a 3D view in Figure 3b. Regions A−C show heights of 6.0, 3.0, and 5.3 nm, respectively. Figure 3c shows the STS spectra acquired on points A−C at 5.8 K. The highest point region has the smallest ZBC, indicating the same tendency as the patterned nanowire case. Temperature-dependent STS measurements were carried out on points A, B, and C within $5.8 \leq T \leq 10.0$ K to understand the correlation between ZBC and critical temperature, as shown in Figure 3d. The depth of the superconducting gap decreases as the temperature increases and vanishes when the temperature reaches T_c. Based on the vanishing superconducting gap, the T_c determined from the spectra on points A, B, and C are about 10.0 9.4, and 10.0 K. However, we observed that the ZBC is different for each point. Point B obtains the lowest T_c with the smallest dip in the ZBC. Meanwhile, point A has the largest dip in ZBC, suggesting that superconductivity is stronger at point A, although its T_c is comparable to that of point C.

We estimated the local variations of microscopic parameters, superconducting gap Δ, thickness h, and grain size and used those as inputs to a model of an inhomogeneous superconductor. The length scale for superconducting variations in the experimental results is around 5 to 15 nm, inferred from to the line profile shown in Figure 2b. Meanwhile, the relative standard deviation of the gap Δ is around 10−20%, based on the estimation of the energy gap (5.4−6.3 meV) from the fwhm of a Gaussian fitted to the STS spectra. Examples of disorder configurations generated using a uniform distribution in the interval $[1\ \xi, 3\ \xi]$ for the domain size d and a normal distribution with mean one and relative standard deviation 0.125 for the gap amplitude $\Delta(\mathbf{r})/\Delta_0$ in nanowires of dimensions $L_1 \times W = 100\ \xi \times 20\ \xi$ are shown in Figure 4a, together with the breakdown of superconductivity by the nucleation of a vortex traversal path just above the critical current. For a disorder realization yielding very low I_c, the modulus of the superconducting order parameter $|\psi|$ typically shows a single line (an example is shown in the second row in the figure), while a realization yielding I_c close to the median (4th row) will usually show 2 or more. This illustrates that disorder configurations that result in a very low I_c are typically dominated by a few very severe defects.

In Figure 4b, the $N = 1$ case shows a histogram of the I_c normalized to the depairing current simulated with the same parameters. It is not practical to extend the system size to much longer wires due to the rapid increase in computational cost. Instead, we may consider a long wire as composed of many smaller segments, each of length $L_1 = 100\ \xi$, and estimate the critical current of the whole length L using extreme value statistics as the minimum of the critical currents of the $N = L/L_1$ segments. The critical current is thus limited by the weakest point along the wire. If L_1 is large enough ($L_1 \gtrsim W$), the I_c of each segment will be uncorrelated and the cumulative distribution of the critical current for the whole wire will be

$$P_N(I_c < x) = 1 - [1 - P_1(I_c < x)]^N \approx 1 - \exp\left(-NP_1(I_c < x)\right) \quad (3)$$

where the latter approximation will hold for a large N. In this way, we are able to estimate the statistics for a much larger geometry with no extra computational cost. For a larger N, the weight of the distribution is shifted toward lower currents and, due to the finite number of disorder realizations simulated, toward poorer statistics. In order to work around this, we have found that a fit of the lower tail ($I_c < I_c^*$) of the cumulative distribution works well, with a function of the form

https://doi.org/10.1021/acsaom.3c00326
ACS Appl. Opt. Mater. 2024, 2, 68−75

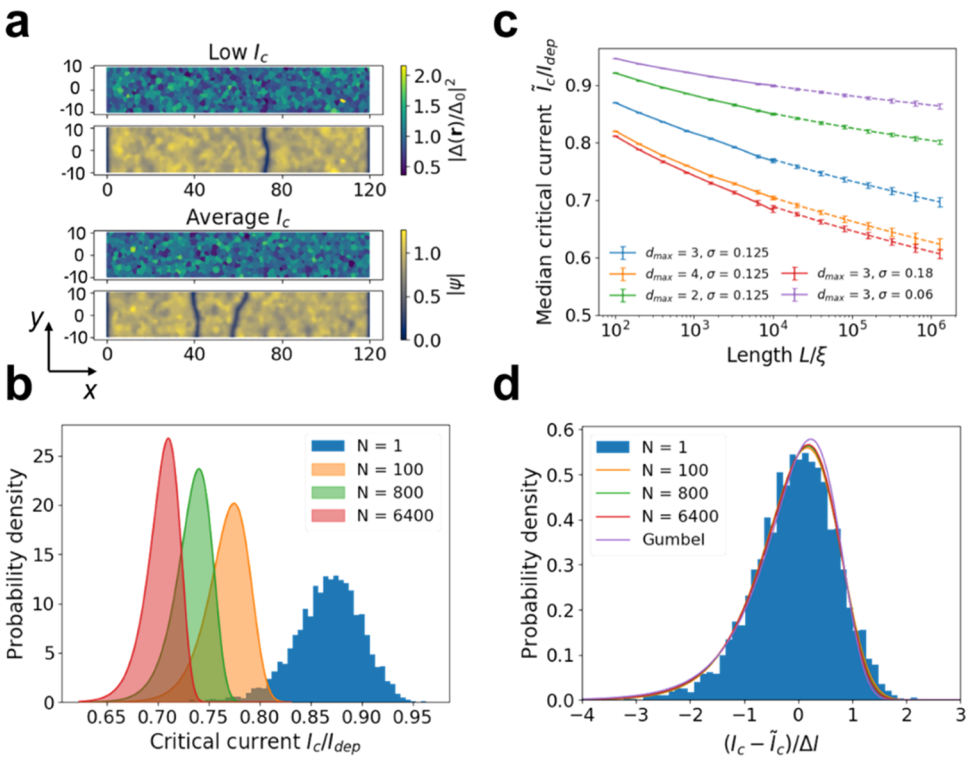

Figure 4. Simulated results. (a) Examples of disorder configurations and modulus $|\psi(r)|$ above the switching current for the case of uniform distribution between 1 and 3 for the domain size and normal distribution with mean 1 and standard deviation $\sigma = 0.125$ for the amplitude for one case of very low I_c and one case of average I_c. (b) Histograms of the simulated critical current normalized to the depairing current for the same distribution. The $N = 1$ case corresponds to the distribution for the simulated length, while $N > 1$ cases show the distribution extrapolated to longer wires. (c) Length dependence of the extrapolated median critical current, normalized to the depairing current. The disorder configuration is generated with uniform $[1, d_{max}]$ distribution for the domain sizes and normal distribution with mean 1 and standard deviation σ. For the solid line, $L < 10^4\ \xi$, the median is calculated directly from the simulated distribution, while for the dashed line, $L > 10^4\ \xi$, the median is calculated for a fit to the simulated distribution. The error bars represent one standard deviation of the calculation of the median obtained using a bootstrap method. (d) Histogram of the same data as shown in (b), where the current is shifted by the median $\tilde{I}_c$ and rescaled by the distance between the quartiles ΔI. The curves collapse on top of each other and show good agreement with the functional form of the Gumbel distribution.

$$\hat{P}_1(I_c < x) = C \ln(2) \exp\left(-(x - I_0)^2/I_1^2\right) \tag{4}$$

where I_0, I_1, and C are fitting parameters. The upper cutoff I_c* for the fit was chosen such that a good fit to the data was obtained in the tail. Using this fitted form, we may extrapolate P_N to much larger values of N, but with this method, there is instead a lower bound for N because the weight of the distribution must lie in the range $I_c < I_c$* for the fit to be valid. Figure 4b shows several resulting histograms of the critical current extrapolated to longer wires. As seen, the typical I_c decreases with increasing length, and the distribution is also getting narrower. The functional form stays rather similar and slowly approaches a Gumbel distribution for longer lengths, as shown in Figure 4d. The median $\tilde{I}_c$ is easily extracted by solving $P_N(\tilde{I}_c) = 0.5$, and is plotted against length $L = NL_1$ in Figure 4c. The error bars represent 1 standard deviation of the median $\tilde{I}_c$ calculated by bootstrap resampling of the initial histogram. The reduction of $\tilde{I}_c$ depends sensitively on both domain size d and magnitude of disorder fluctuations σ in a nonlinear way. As shown in Figure 4c the median $\tilde{I}_c$ depends almost logarithmically on the length of the wire, similar to previously reported results.[22,23] The deviation from a pure logarithmic dependence can be analyzed in the regime of a moderately large N where the fitted function $\hat{P}_1$ is valid. In this regime, we can invert the expression for P_N to find the analytical form of the median

$$\tilde{I}_c \approx I_0 - I_1\sqrt{\ln(CN)} \tag{5}$$

A similar calculation shows that the width of the distribution decreases approximately as $1/\sqrt{\ln(CN)}$. As an example, for the parameters of Figure 4, the simulations show that these kinds of inhomogeneities in a wire of length $L = 10^5\ \xi \approx 500\ \mu$m can lead to a reduction of the typical values of the critical current by about 25%.

To assess these theoretical findings, the critical current I_c of 100 nm wide NbTiN nanowires with different lengths was measured. This corresponds to the simulated case of a 5 nm coherence length and nanowire width of 20 coherence lengths. Four devices for 5 and 500 μm lengths were tested, resulting in $I_c = 44.2 \pm 2.2\ \mu$A and $I_c = 42.1 \pm 1.1\ \mu$A, respectively. The experimentally observed reduction of around 5% for a hundred-fold length increase is generally in line with the theoretical predictions for some of the used parameters (see blue and green curves in Figure 4c), validating the presented model and, hence, providing quantitative statistical values for NbTiN inhomogeneity.

CONCLUSIONS

In summary, our study using STM/STS measurements revealed the inhomogeneous superconducting behavior of NbTiN nanowires in SNSPDs. We have identified the inhomogeneity of T_c in the film and its strong correlation to

https://doi.org/10.1021/acsaom.3c00326
ACS Appl. Opt. Mater. 2024, 2, 68−75

the local film thickness through temperature-dependent STS imaging. We have also demonstrated, using theoretical calculations and experimental data, that this inhomogeneity in the NbTiN film has a significant impact on the critical currents of the nanowire devices. Our findings shed light on the intricate properties of superconducting materials utilized in advanced quantum devices and hold important implications for the development of future quantum technologies.

■ ASSOCIATED CONTENT

Supporting Information

The Supporting Information is available free of charge at https://pubs.acs.org/doi/10.1021/acsaom.3c00326.

NbTiN from an optical spectroscope and CCD in STM; the large-scale image of NbTiN thin film (PDF)

■ AUTHOR INFORMATION

Corresponding Authors

Val Zwiller − *Quantum Nano Photonics Group, Department of Applied Physics, Royal Institute of Technology (KTH), Stockholm 10691, Sweden*; Email: zwiller@kth.se

Chun-Liang Lin − *Department of Electrophysics, National Yang Ming Chiao Tung University, Hsinchu 30010, Taiwan*; orcid.org/0000-0001-8781-3650; Email: clin@nycu.edu.tw

Authors

Pei-Jung Chen − *Department of Electrophysics, National Yang Ming Chiao Tung University, Hsinchu 30010, Taiwan*

Guan-Hao Chen − *Department of Electrophysics, National Yang Ming Chiao Tung University, Hsinchu 30010, Taiwan; Research Center for Applied Sciences, Academia Sinica, Taipei 11529, Taiwan*

Robert Vedin − *Department of Physics, KTH Royal Institute of Technology, 10691 Stockholm, Sweden*

Mattias Jönsson − *Department of Physics, KTH Royal Institute of Technology, 10691 Stockholm, Sweden*; orcid.org/0000-0001-8488-9035

Samuel Gyger − *Quantum Nano Photonics Group, Department of Applied Physics, Royal Institute of Technology (KTH), Stockholm 10691, Sweden*; orcid.org/0000-0003-2080-9897

Stephan Steinhauer − *Quantum Nano Photonics Group, Department of Applied Physics, Royal Institute of Technology (KTH), Stockholm 10691, Sweden*; orcid.org/0000-0001-6875-6849

Juhn-Jong Lin − *Department of Electrophysics, National Yang Ming Chiao Tung University, Hsinchu 30010, Taiwan; Center for Emergent Functional Matter Science (CEFMS), National Yang Ming Chiao Tung University, Hsinchu 30010, Taiwan*

Wen-Hao Chang − *Department of Electrophysics, National Yang Ming Chiao Tung University, Hsinchu 30010, Taiwan; Research Center for Applied Sciences, Academia Sinica, Taipei 11529, Taiwan; Center for Emergent Functional Matter Science (CEFMS), National Yang Ming Chiao Tung University, Hsinchu 30010, Taiwan*; orcid.org/0000-0003-4880-6006

Jack Lidmar − *Department of Physics, KTH Royal Institute of Technology, 10691 Stockholm, Sweden*; orcid.org/0000-0002-9881-7857

Complete contact information is available at: https://pubs.acs.org/10.1021/acsaom.3c00326

Author Contributions

C.-L.L., W.-H.C., V.Z., and J.L. conceived and supervised the project, P.-J.C. and G.-H.C. performed the STM characterization and data analysis, S.G. and S.S. fabricated the samples, R.V. and M.J. performed the theoretical calculations, J.-J.L. contributed to the discussion. The text was initially composed by P.-J.C., R.V., and C.-L.L. with input from all coauthors. All coauthors further contributed to the discussion of the experimental work and the final version of the manuscript.

Notes

The authors declare no competing financial interest.

■ ACKNOWLEDGMENTS

This work was financially supported by the "Center for the Semiconductor Technology Research" from The Featured Areas Research Center Program within the framework of the Higher Education Sprout Project by the Ministry of Education (MOE) in Taiwan and also supported in part by the National Science and Technology Council, Taiwan, under Grant NSTC 110-2634-F-009-027, 110-2112-M-A49-013-MY3, NSTC 110-2112-M-A49-022-MY2, and NSTC 111-2923-M-A49-003. The computations were enabled by resources provided by the Swedish National Infrastructure for Computing (SNIC) at HPC2N partially funded by the Swedish Research Council through grant agreement no. 2018-05973.

■ REFERENCES

(1) Arute, F.; Arya, K.; Babbush, R.; Bacon, D.; Bardin, J. C.; Barends, R.; Biswas, R.; Boixo, S.; Brandao, F. G. S. L.; Buell, D. A.; Burkett, B.; Chen, Y.; Chen, Z.; Chiaro, B.; Collins, R.; Courtney, W.; Dunsworth, A.; Farhi, E.; Foxen, B.; Fowler, A.; Gidney, C.; Giustina, M.; Graff, R.; Guerin, K.; Habegger, S.; Harrigan, M. P.; Hartmann, M. J.; Ho, A.; Hoffmann, M.; Huang, T.; Humble, T. S.; Isakov, S. V.; Jeffrey, E.; Jiang, Z.; Kafri, D.; Kechedzhi, K.; Kelly, J.; Klimov, P. V.; Knysh, S.; Korotkov, A.; Kostritsa, F.; Landhuis, D.; Lindmark, M.; Lucero, E.; Lyakh, D.; Mandrà, S.; McClean, J. R.; McEwen, M.; Megrant, A.; Mi, X.; Michielsen, K.; Mohseni, M.; Mutus, J.; Naaman, O.; Neeley, M.; Neill, C.; Niu, M. Y.; Ostby, E.; Petukhov, A.; Platt, J. C.; Quintana, C.; Rieffel, E. G.; Roushan, P.; Rubin, N. C.; Sank, D.; Satzinger, K. J.; Smelyanskiy, V.; Sung, K. J.; Trevithick, M. D.; Vainsencher, A.; Villalonga, B.; White, T.; Yao, Z. J.; Yeh, P.; Zalcman, A.; Neven, H.; Martinis, J. M. Quantum Supremacy Using a Programmable Superconducting Processor. *Nature* **2019**, *574* (7779), 505−510.

(2) Wu, Y.; Bao, W.-S.; Cao, S.; Chen, F.; Chen, M.-C.; Chen, X.; Chung, T.-H.; Deng, H.; Du, Y.; Fan, D.; Gong, M.; Guo, C.; Guo, C.; Guo, S.; Han, L.; Hong, L.; Huang, H.-L.; Huo, Y.-H.; Li, L.; Li, N.; Li, S.; Li, Y.; Liang, F.; Lin, C.; Lin, J.; Qian, H.; Qiao, D.; Rong, H.; Su, H.; Sun, L.; Wang, L.; Wang, S.; Wu, D.; Xu, Y.; Yan, K.; Yang, W.; Yang, Y.; Ye, Y.; Yin, J.; Ying, C.; Yu, J.; Zha, C.; Zhang, C.; Zhang, H.; Zhang, K.; Zhang, Y.; Zhao, H.; Zhao, Y.; Zhou, L.; Zhu, Q.; Lu, C.-Y.; Peng, C.-Z.; Zhu, X.; Pan, J.-W. Strong Quantum Computational Advantage Using a Superconducting Quantum Processor. *Phys. Rev. Lett.* **2021**, *127* (18), No. 180501.

(3) Zhong, H.-S.; Wang, H.; Deng, Y.-H.; Chen, M.-C.; Peng, L.-C.; Luo, Y.-H.; Qin, J.; Wu, D.; Ding, X.; Hu, Y.; Hu, P.; Yang, X.-Y.; Zhang, W.-J.; Li, H.; Li, Y.; Jiang, X.; Gan, L.; Yang, G.; You, L.; Wang, Z.; Li, L.; Liu, N.-L.; Lu, C.-Y.; Pan, J.-W. Quantum Computational Advantage Using Photons. *Science* **2020**, *370*, 1460−1463.

(4) Jackson, D. M.; Gangloff, D. A.; Bodey, J. H.; Zaporski, L.; Bachorz, C.; Clarke, E.; Hugues, M.; Le Gall, C.; Atatüre, M.

Quantum Sensing of a Coherent Single Spin Excitation in a Nuclear Ensemble. *Nat. Phys.* **2021**, *17* (5), 585−590.
(5) Bhaskar, M. K.; Riedinger, R.; Machielse, B.; Levonian, D. S.; Nguyen, C. T.; Knall, E. N.; Park, H.; Englund, D.; Lončar, M.; Sukachev, D. D.; Lukin, M. D. Experimental Demonstration of Memory-Enhanced Quantum Communication. *Nature* **2020**, *580* (7801), 60−64.
(6) Reddy, D. V.; Nerem, R. R.; Nam, S. W.; Mirin, R. P.; Verma, V. B. Superconducting Nanowire Single-Photon Detectors with 98% System Detection Efficiency at 1550 nm. *Optica* **2020**, *7* (12), 1649.
(7) Chang, J.; Los, J. W. N.; Tenorio-Pearl, J. O.; Noordzij, N.; Gourgues, R.; Guardiani, A.; Zichi, J. R.; Pereira, S. F.; Urbach, H. P.; Zwiller, V.; Dorenbos, S. N.; Esmaeil Zadeh, I. Detecting Telecom Single Photons with 99.5−2.07 + 0.5% System Detection Efficiency and High Time Resolution. *APL Photonics* **2021**, *6* (3), No. 036114.
(8) Korzh, B.; Zhao, Q.-Y.; Allmaras, J. P.; Frasca, S.; Autry, T. M.; Bersin, E. A.; Beyer, A. D.; Briggs, R. M.; Bumble, B.; Colangelo, M.; Crouch, G. M.; Dane, A. E.; Gerrits, T.; Lita, A. E.; Marsili, F.; Moody, G.; Peña, C.; Ramirez, E.; Rezac, J. D.; Sinclair, N.; Stevens, M. J.; Velasco, A. E.; Verma, V. B.; Wollman, E. E.; Xie, S.; Zhu, D.; Hale, P. D.; Spiropulu, M.; Silverman, K. L.; Mirin, R. P.; Nam, S. W.; Kozorezov, A. G.; Shaw, M. D.; Berggren, K. K. Demonstration of Sub-3 Ps Temporal Resolution with a Superconducting Nanowire Single-Photon Detector. *Nat. Photonics* **2020**, *14* (4), 250−255.
(9) Schuck, C.; Pernice, W. H. P.; Tang, H. X. Waveguide Integrated Low Noise NbTiN Nanowire Single-Photon Detectors with Milli-Hz Dark Count Rate. *Sci. Rep.* **2013**, *3* (1), No. 1893.
(10) Mueller, A. S.; Korzh, B.; Runyan, M.; Wollman, E. E.; Beyer, A. D.; Allmaras, J. P.; Velasco, A. E.; Craiciu, I.; Bumble, B.; Briggs, R. M.; Narvaez, L.; Peña, C.; Spiropulu, M.; Shaw, M. D. Free-Space Coupled Superconducting Nanowire Single-Photon Detector with Low Dark Counts. *Optica* **2021**, *8* (12), 1586−1587.
(11) Yan, R.; Khalsa, G.; Vishwanath, S.; Han, Y.; Wright, J.; Rouvimov, S.; Katzer, D. S.; Nepal, N.; Downey, B. P.; Muller, D. A.; Xing, H. G.; Meyer, D. J.; Jena, D. GaN/NbN Epitaxial Semiconductor/Superconductor Heterostructures. *Nature* **2018**, *555* (7695), 183−189.
(12) Mercier, F.; Coindeau, S.; Lay, S.; Crisci, A.; Benz, M.; Encinas, T.; Boichot, R.; Mantoux, A.; Jimenez, C.; Weiss, F.; Blanquet, E. Niobium nitride thin films deposited by high temperature chemical vapor deposition. *Surf. Coat. Technol.* **2014**, *260*, 126−132.
(13) Cheng, R.; Wang, S.; Tang, H. X. Superconducting Nanowire Single-Photon Detectors Fabricated from Atomic-Layer-Deposited NbN. *Appl. Phys. Lett.* **2019**, *115* (24), No. 241101.
(14) Matsunaga, T.; Maezawa, H.; Noguchi, T. Characterization of NbTiN Thin Films Prepared by Reactive DC-Magnetron Sputtering. *IEEE Trans. Appl. Supercond.* **2003**, *13* (2), 3284−3287.
(15) Baturina, T. I.; Mironov, A. Yu.; Vinokur, V. M.; Baklanov, M. R.; Strunk, C. Localized Superconductivity in the Quantum-Critical Region of the Disorder-Driven Superconductor-Insulator Transition in TiN Thin Films. *Phys. Rev. Lett.* **2007**, *99* (25), No. 257003.
(16) Mondal, M.; Kamlapure, A.; Chand, M.; Saraswat, G.; Kumar, S.; Jesudasan, J.; Benfatto, L.; Tripathi, V.; Raychaudhuri, P. Phase Fluctuations in a Strongly Disordered *s*-Wave NbN Superconductor Close to the Metal-Insulator Transition. *Phys. Rev. Lett.* **2011**, *106* (4), No. 047001.
(17) Sacépé, B.; Chapelier, C.; Baturina, T. I.; Vinokur, V. M.; Baklanov, M. R.; Sanquer, M. Disorder-Induced Inhomogeneities of the Superconducting State Close to the Superconductor-Insulator Transition. *Phys. Rev. Lett.* **2008**, *101* (15), No. 157006.
(18) Kamlapure, A.; Das, T.; Ganguli, S. C.; Parmar, J. B.; Bhattacharyya, S.; Raychaudhuri, P. Emergence of Nanoscale Inhomogeneity in the Superconducting State of a Homogeneously Disordered Conventional Superconductor. *Sci. Rep.* **2013**, *3* (1), No. 2979.
(19) Noat, Y.; Cherkez, V.; Brun, C.; Cren, T.; Carbillet, C.; Debontridder, F.; Ilin, K.; Siegel, M.; Semenov, A.; Hübers, H.-W.; Roditchev, D. Unconventional Superconductivity in Ultrathin Superconducting NbN Films Studied by Scanning Tunneling Spectroscopy. *Phys. Rev. B* **2013**, *88* (1), No. 014503.
(20) Larkin, A. I.; Ovchinnikov, Y. N. Influence of Inhomogeneous on Superconductor Properties. *Soviet Phys. - JETP* **1972**, *34* (3), 651.
(21) Budinská, B.; Aichner, B.; Vodolazov, D. Yu.; Mikhailov, M. Yu.; Porrati, F.; Huth, M.; Chumak, A. V.; Lang, W.; Dobrovolskiy, O. V. Rising Speed Limits for Fluxons via Edge-Quality Improvement in Wide MoSi Thin Films. *Phys. Rev. Appl.* **2022**, *17*, No. 034072.
(22) Gaudio, R.; op 't Hoog, K. P. M.; Zhou, Z.; Sahin, D.; Fiore, A. Inhomogeneous Critical Current in Nanowire Superconducting Single-Photon Detectors. *Appl. Phys. Lett.* **2014**, *105* (22), No. 222602.
(23) Yang, X.; You, L.; Zhang, L.; Lv, C.; Li, H.; Liu, X.; Zhou, H.; Wang, Z. Comparison of Superconducting Nanowire Single-Photon Detectors Made of NbTiN and NbN Thin Films. *IEEE Trans. Appl. Supercond.* **2018**, *28* (1), 1−6.
(24) Kooi, J. W.; Stern, J. A.; Chattopadhyay, G.; LeDuc, H. G.; Bumble, B.; Zmuidzinas, J. Low-Loss NbTiN Films for THz SIS Mixer Tuning Circuits. *Int. J. Infrared Millimeter Waves* **1998**, *19* (3), 373−383.
(25) Takeda, M.; Shan, W.; Kojima, T.; Uzawa, Y.; Kroug, M.; Li, J.; Shi, S.; Wang, Z. Mixing Properties of NbN-Based SIS Mixers With NbTiN Wirings. *IEEE Trans. Appl. Supercond.* **2009**, *19* (3), 436−439.
(26) Samkharadze, N.; Bruno, A.; Scarlino, P.; Zheng, G.; DiVincenzo, D. P.; DiCarlo, L.; Vandersypen, L. M. K. High Kinetic Inductance Superconducting Nanowire Resonators for Circuit QED in a Magnetic Field. *Phys. Rev. Appl.* **2016**, *5* (4), No. 044004.
(27) Müller, M.; Luschmann, T.; Faltermeier, A.; Weichselbaumer, S.; Koch, L.; Huber, G. B. P.; Schumacher, H. W.; Ubbelohde, N.; Reifert, D.; Scheller, T.; Deppe, F.; Marx, A.; Filipp, S.; Althammer, M.; Gross, R.; Huebl, H. Magnetic Field Robust High Quality Factor NbTiN Superconducting Microwave Resonators. *Mater. Quantum Technol.* **2022**, *2* (1), No. 015002.
(28) Esmaeil Zadeh, I.; Los, J. W. N.; Gourgues, R. B. M.; Steinmetz, V.; Bulgarini, G.; Dobrovolskiy, S. M.; Zwiller, V.; Dorenbos, S. N. Single-Photon Detectors Combining High Efficiency, High Detection Rates, and Ultra-High Timing Resolution. *APL Photonics* **2017**, *2* (11), No. 111301.
(29) Esmaeil Zadeh, I.; Chang, J.; Los, J. W. N.; Gyger, S.; Elshaari, A. W.; Steinhauer, S.; Dorenbos, S. N.; Zwiller, V. Superconducting Nanowire Single-Photon Detectors: A Perspective on Evolution, State-of-the-Art, Future Developments, and Applications. *Appl. Phys. Lett.* **2021**, *118* (19), No. 190502.
(30) Sidorova, M.; Semenov, A. D.; Hübers, H.-W.; Gyger, S.; Steinhauer, S.; Zhang, X.; Schilling, A. Magnetoconductance and Photoresponse Properties of Disordered NbTiN Films. *Phys. Rev. B* **2021**, *104* (18), No. 184514.
(31) Hong, T.; Choi, K.; Ik Sim, K.; Ha, T.; Cheol Park, B.; Yamamori, H.; Hoon Kim, J. Terahertz Electrodynamics and Superconducting Energy Gap of NbTiN. *J. Appl. Phys.* **2013**, *114* (24), No. 243905.
(32) Chen, S.-Z.; Yang, J.-W.; Peng, T.-Y.; Chu, Y.-C.; Yeh, C.-C.; Hu, I.-F.; Mhatre, S.; Lu, Y.-J.; Liang, C.-T. Disorder-Induced 2D Superconductivity in a NbTiN Film Grown on Si by Ultrahigh-Vacuum Magneton Sputtering. *Supercond. Sci. Technol.* **2022**, *35* (6), No. 064003.
(33) Driessen, E. F. C.; Coumou, P. C. J. J.; Tromp, R. R.; de Visser, P. J.; Klapwijk, T. M. Strongly Disordered TiN and NbTiN *s*-Wave Superconductors Probed by Microwave Electrodynamics. *Phys. Rev. Lett.* **2012**, *109* (10), No. 107003.
(34) Zichi, J.; Chang, J.; Steinhauer, S.; von Fieandt, K.; Los, J. W. N.; Visser, G.; Kalhor, N.; Lettner, T.; Elshaari, A. W.; Zadeh, I. E.; Zwiller, V. Optimizing the Stoichiometry of Ultrathin NbTiN Films for High-Performance Superconducting Nanowire Single-Photon Detectors. *Opt. Express* **2019**, *27* (19), 26579−26587.
(35) Kramer, L.; Watts-Tobin, R. J. Theory of Dissipative Current-Carrying States in Superconducting Filaments. *Phys. Rev. Lett.* **1978**, *40* (15), 1041.

https://doi.org/10.1021/acsaom.3c00326
ACS Appl. Opt. Mater. 2024, 2, 68−75

(36) Watts-Tobin, R. J.; Krähenbühl, Y.; Kramer, L. Nonequilibrium Theory of Dirty, Current-Carrying Superconductors: Phase-slip Oscillators in Narrow Filaments Near Tc. *J. Low Temp. Phys.* **1981**, *42* (5), 459.
(37) Kopnin, N. *Theory of Nonequilibrium Superconductivity*; Oxford University Press, 2001.
(38) Hart, K. A.; Rimoli, J. J. Generation of Statistically Representative Microstructures with Direct Grain Geometry Control. *Comput. Methods Appl. Mech. Eng.* **2020**, *370*, No. 113242.
(39) Hart, K. A.; Rimoli, J. J. MicroStructPy: A Statistical Microstructure Mesh Generator in Python. *SoftwareX* **2020**, *12*, No. 100595.
(40) Jönsson, M.; Vedin, R.; Gyger, S.; Sutton, J. A.; Steinhauer, S.; Zwiller, V.; Wallin, M.; Lidmar, J. Current Crowding in Nanoscale Superconductors within the Ginzburg-Landau Model. *Phys. Rev. Appl.* **2022**, *17* (6), No. 064046.
(41) Steinhauer, S.; Yang, L.; Gyger, S.; Lettner, T.; Errando-Herranz, C.; Jöns, K. D.; Baghban, M. A.; Gallo, K.; Zichi, J.; Zwiller, V. NbTiN Thin Films for Superconducting Photon Detectors on Photonic and Two-Dimensional Materials. *Appl. Phys. Lett.* **2020**, *116* (17), No. 171101.
(42) Bouadim, K.; Loh, Y. L.; Randeria, M.; Trivedi, N. Single- and two-particle energy gaps across the disorder-driven superconductor–insulator transition. *Nat. Phys.* **2011**, *7*, 884–889.

https://doi.org/10.1021/acsaom.3c00326
ACS Appl. Opt. Mater. 2024, 2, 68–75